



1 Photochemistry on the underside of the mesospheric Na layer

2 Tao Yuan<sup>1,2</sup>, Wuhu Feng<sup>3,4</sup>, John M. C. Plane<sup>3</sup>, Daniel R. Marsh<sup>3,5</sup>

3 1. Physics Department, Utah State University, Logan, Utah, USA

4 2. Center for Atmospheric and Space Sciences, Utah State University, Logan, Utah, USA

5 3. School of Chemistry, University of Leeds, Leeds, UK

6 4. National Centre for Atmospheric Science, University of Leeds, Leeds, UK

7 5. National Center for Atmospheric Research, Boulder, Colorado, USA

## 8 **Abstract**

9 Lidar observations of the mesospheric Na layer have revealed considerable diurnal variations  
10 particularly on the underside of the main layer where more than an order-of-magnitude increase of Na  
11 density has been observed below 80 km after sunrise. In this paper, multi-year Na lidar observations over  
12 a full diurnal cycle at Utah State University (USU) (41.8°N, 111.8°W) and a global atmospheric model of  
13 Na with 0.5 km vertical resolution in the mesosphere lower thermosphere (WACCM-Na) are utilized to  
14 explore the dramatic changes of Na density on the layer underside. Photolysis of the principal reservoir  
15 NaHCO<sub>3</sub> is shown to be primarily responsible for the increase in Na after sunrise, amplified by the  
16 increased rate of reaction of NaHCO<sub>3</sub> with atomic H, which is mainly produced from the photolysis of  
17 H<sub>2</sub>O and the reaction of OH with O<sub>3</sub>. This finding is further supported by Na lidar observation at USU  
18 during the solar eclipse (> 96% totality) event on August 21<sup>st</sup>, 2017, when a decrease and recovery of the  
19 Na density on the underside of the layer were observed. Lastly, the model simulation shows that the Fe  
20 density underside around 80 km increases larger and earlier than observed Na changes during sunrise  
21 because of the considerably faster photolysis rate of its major reservoir FeOH.

## 22 **1. Introduction**

23 The layer of Na atoms in the upper mesosphere and lower thermosphere (MLT, ~ 80-105 km in  
24 altitude), is formed naturally by meteoric ablation along with other metallic layers such as Fe, Mg, Ca  
25 and K [Plane et al., 2015]. The climatological variations of this Na layer are known to be mainly  
26 controlled by a series of chemical reactions and dynamics, including tides, gravity waves and the mean  
27 circulation in the MLT [Plane, 2004, Marsh et al., 2013]. Mesospheric Na atoms are an important tracer  
28 in the MLT, where they are observed by resonance fluorescence, either by the lidar technique [Krueger et



29 al., 2015] or solar-pumped dayglow from space [Fan et al., 2007]. The Na lidar technique has enabled  
30 high temporal and spatial resolution measurements of the mesospheric Na layer since the 1970s  
31 [Sandford and Gibson, 1970]. In addition to Na density observations, Na temperature/wind lidars can  
32 measure the atmospheric temperature and wind fields over full diurnal cycle by observing Doppler  
33 broadening and shifting of the hyperfine structure of one of the Na D lines [Krueger et al., 2015].  
34 Atmospheric observations have been complemented by laboratory kinetic studies of the important  
35 reactions which control both the neutral and ion-molecule chemistry of Na in the MLT [Plane, 1999;  
36 2004; Plane et al., 2015], and the development of atmospheric models which satisfactorily reproduce  
37 seasonal observations over most latitudes [Plane, 2004; Marsh et al., 2013; Li et al., 2018]

38         However, less detailed work has been done to investigate the diurnal variations in Na density,  
39 especially on the underside of the layer where neutral chemistry dominates. Advances in lidar technology  
40 have enabled Na density observations over a full diurnal cycle [Chen et al., 1996; States and Gardner,  
41 1999; Clemesha et al., 2002; Yuan et al., 2012]. Utilizing multi-year observations, Yuan et al. (2012)  
42 investigated the diurnal variation and tidal period perturbations of the Na density. These tidal Na  
43 perturbations were then used to estimate the tidal vertical wind perturbations [Yuan et al., 2014], showing  
44 that, although closely correlated with tidal waves and dominated by tidal wave modulations in the lower  
45 thermosphere, the Na diurnal and semidiurnal variations cannot be induced by tidal modulations alone.  
46 This is especially the case on the underside of the layer below ~ 90 km, where tidal wave amplitudes are  
47 relatively small (see Figure 5a and 5b in Yuan et al., 2012), implying that other mechanisms make a  
48 significant contribution to the diurnal variation of the Na layer underside.

49         Plane et al. (1999) recognized the important role of photochemical reactions in the characterizing  
50 the underside of the Na layer, and then measured the photolysis cross sections of several Na-containing  
51 molecules – NaO, NaO<sub>2</sub>, NaOH and NaHCO<sub>3</sub>, which models show are significant mesospheric reservoir  
52 species [Self and Plane, 2002, Marsh et al., 2013]. These cross sections, measured at temperatures  
53 appropriate to the MLT, were then used to calculate mesospheric photolysis rates:



54	$\text{NaO} + h\nu \rightarrow \text{Na} + \text{O}$	$5.5 \times 10^{-2} \text{ s}^{-1}$	R1
55	$\text{NaO}_2 + h\nu \rightarrow \text{Na} + \text{O}_2$	$1.9 \times 10^{-2} \text{ s}^{-1}$	R2
56	$\text{NaOH} + h\nu \rightarrow \text{Na} + \text{OH}$	$1.8 \times 10^{-2} \text{ s}^{-1}$	R3
57	$\text{NaHCO}_3 + h\nu \rightarrow \text{Na} + \text{HCO}_3$	$1.3 \times 10^{-4} \text{ s}^{-1}$	R4

58           These *direct* photochemical reactions release atomic Na during daytime. Furthermore, *indirect*  
59 photochemistry also plays a role. The photolysis of O<sub>2</sub>, O<sub>3</sub> and H<sub>2</sub>O [Brasseur and Solomon, 2005] lead  
60 to the production of H and O (R5 – R8), increasing their concentrations by more than 1 order of  
61 magnitude during daytime at an altitude around 80 km [Plane, 2003]. The daily variation of H is further  
62 facilitated by the reactions between HO<sub>2</sub> and O/O<sub>3</sub>, which has strong diurnal variations.

63	$\text{O}_2 + h\nu \rightarrow 2\text{O}$		R5
64	$\text{O}_3 + h\nu \rightarrow \text{O} + \text{O}_2$		R6
65	$\text{H}_2\text{O} + h\nu \rightarrow \text{H} + \text{OH}$		R7
66	$\text{OH} + \text{O} \rightarrow \text{H} + \text{O}_2$		R8
67	$\text{NaHCO}_3 + \text{H} \rightarrow \text{Na} + \text{H}_2\text{CO}_3$		R9

68 Thus, H and O reduce these Na compounds listed above to atomic Na [Plane, 2004].

69           To demonstrate the effect of solar radiation on mesospheric Na layer, including R1-R8, Figure 1  
70 shows the averaged Na density variation in the layer between 75 km and 105 km during a 6-hour period  
71 that straddles sunrise (from 3 hours before to 3 hours after sunrise) in the fall season (from August 20 to  
72 September 30). The results are based on 50 days of Na lidar observations at USU (41.8°N, 111.8°W)  
73 between 2011 and 2016. Figure 1 also includes the ratio profile between the Na density 3 hours after  
74 sunrise to that 3 hours before sunrise. The lidar observations clearly show that, while there is an overall  
75 Na density increase after sunrise below ~ 92 km, the increase at and below 80 km is much larger than



76 closer to the layer peak: the Na density increases by a factor of  $\sim 6$  at 80 km and  $\sim 40$  near 78 km,  
77 whereas it is almost uncharged around  $\sim 95$  km. The dramatic oscillation of the ratio below 78 km is due  
78 to very low Na density before sunrise (usually below  $1 \text{ cm}^{-3}$ ). Note that this ratio calculation for Na  
79 density profiles 1 hour before and 1 hour after sunrise generates a similar ratio profile, which  
80 demonstrated even larger ratio near 80 km, a factor of  $\sim 20$ . This implicates very quick Na density  
81 enhancement during the process of sunrise. This analysis therefore provides strong evidence for the  
82 impact of photochemistry on the underside of the Na layer.

83 In this paper we compare the USU Na lidar diurnal cycle observations of mesospheric Na layer  
84 during a continuous 7-day campaign in fall 2012 with the Na density variation simulated by NCAR's  
85 Whole Atmosphere Community Climate Model with Na chemistry (WACCM-Na) [Marsh et al., 2013] at  
86 the USU location during the same period, in order to investigate quantitatively the role of photochemistry  
87 on the Na layer. In addition, Fe density variation by the latest WACCM-Fe [Feng et al., 2017] due to  
88 photolysis is also discussed to show the distinct feature of the Fe in the underside of the main layer. The  
89 Na Lidar measurements made during the solar eclipse on August 21, 2017 in North America are then  
90 used as a further robust test of the role of photolysis.

## 91 **2. Instrument and Model description**

92 The USU Na Temperature/Wind lidar system, originally developed at Colorado State University, has  
93 been operating at the USU main campus since summer 2010. In addition to Na density observations,  
94 neutral temperature and winds are also measured for the mesopause region ( $\sim 80$ -110 km) [Krueger et al.,  
95 2015]. The lidar return signals can be recorded in 150 m bins in the line-of-sight direction, and saved  
96 every minute. Facilitated by a pair of customized Faraday filters deployed at its receiver [Harrell et al.,  
97 2009], this advanced lidar system can also reject the sky background significantly during daytime, while  
98 receiving the Na echo with minimum loss. This technique provides robust measurements of these  
99 important atmospheric parameters under sunlight condition, thereby enabling this investigation of Na  
100 photochemistry. In this study, we focus on two sets of Na lidar data: Na density data taken between UT



101 Day 271 (September 27) and UT Day 277 (October 3) of 2012 and lidar observations during the solar  
102 eclipse on August 21, 2017. The lidar observations presented here are processed with 2-km vertical  
103 resolution, and 10-minute and 30-minute temporal resolution for nighttime and daytime data,  
104 respectively, to achieve appropriate signal to noise (S/N) for studying the underside of the layer between  
105 75 and 80 km, where the Na density is low ( $<100 \text{ cm}^{-3}$ ). The lidar observations during the solar eclipse  
106 are processed with 10-minute resolution to investigate the potential eclipse-induced perturbations in  
107 detail.

108 WACCM-Na is a global meteoric Na model which satisfactorily reproduces lidar and satellite  
109 measurements of the Na layer [e.g., Marsh et al., 2013; Dunker et al., 2015; Plane et al., 2015; Langowski  
110 et al., 2017; Dawkins et al., 2016; Feng et al., 2017]. WACCM-Na uses the Community Earth System  
111 Model (version 1) framework (e.g., Hurrell et al., 2013), which includes detailed physical processes as  
112 described in the Community Atmosphere Model, version 4 (CAM4) [Neale et al., 2012], and has the fully  
113 interactive chemistry described in Kinnison et al. (2007). The current configuration for WACCM is based  
114 on a finite volume dynamical core [Lin, 2004] for tracer advection. For the present study, we used a  
115 specific dynamics (SD) version of WACCM, in which winds and temperatures below 50-60 km are  
116 nudged towards NASA's Modern-Era Retrospective Analysis for Research and Applications (MERRA)  
117 [Lamarque et al., 2012]. The horizontal resolution is  $1.9^\circ$  latitude  $\times$   $2.5^\circ$  longitude. For this study we  
118 performed model experiments using two different vertical resolution: 88 and 144 vertical model levels  
119 (termed as lev88 and lev144), both have the same 62 vertical levels from surface to 0.42 Pa (below  $\sim$ 50  
120 km) as MERRA with different vertical resolution above 0.42 Pa (ie., lev88 which has been used as a  
121 standard SD-WACCM gives a coarse height resolution from  $\sim$ 1.9 to  $\sim$ 3.5 km above the upper  
122 stratosphere to MLT while lev144 has fine vertical resolution increases from 1.9 km down to around 500  
123 m in the MLT [Merkel et al., 2009; Viehl et al., 2016]. The Na reaction scheme described in Plane et al.  
124 (2015) is updated with the results of recent laboratory studies [Gomez-Martin et al., 2016; 2017], and the  
125 meteoric input function (MIF) of Na from Cárriillo-Sanchez et al. (2016) is used. Note that the absolute  
126 Na MIF used in this paper is the same as in Li et al. (2018) and Plane et al. (2018); i.e., it has been



127 divided by a factor of 5 from the MIF in Cártillo-Sánchez et al. (2016), to match the observations. In  
128 order to contrast the photochemical behavior of the Na layer underside with that of the Fe layer, a  
129 WACCM-Fe simulation was also performed. The model output was sampled over USU (41.8°N,  
130 111.8°W) every thirty minutes (the model time step) then interpolated to the same observational period  
131 for the available lidar daytime measurements for direct comparisons (note that the modelled nighttime  
132 uses the same daytime because the model time step is every 30 minutes while the lidar nighttime  
133 measurement is every 10 minutes).

### 134 3. Comparison of the Na lidar observations with WACCM-Na

135 The averaged Na density diurnal variation calculated from the intensive 7-day USU Na lidar  
136 campaign is presented as the top plot in Figure 2. During the campaign, the time of sunrise in the MLT is  
137 around 06:56 local time (LT) based on solar elevation angle ( $-5^\circ$  represents sunrise in the MLT); the noon  
138 and sunset times are 13:45 LT and 20:35 LT, respectively. The observations reveal strong variations  
139 within the layer during the day. Close to the layer peak there are three minima at around 20:00 LT  
140 (evening), 04:00 LT (right before dawn) and 16:00 LT (afternoon), where the Na density falls to ~  
141  $3000/\text{cm}^3$ . These are separated by two significant maxima near 91 km: the stronger occurs right after  
142 sunrise and lasts almost the whole morning with a peak density more than  $4400/\text{cm}^3$ ; the other maximum  
143 occurs near 22:00 LT (shortly before midnight), and has a much shorter lifetime (~ 1 hour) with peak  
144 density slightly above  $4100/\text{cm}^3$ . Similar to Figure 1, on the underside of the main layer there is clear  
145 evidence of an increase of Na density after sunrise.

146 Compared with the lidar observations, Figure 2 (middle panel) shows that the relatively coarse  
147 resolution WACCM-Na produces a reasonable Na layer in terms of a peak Na density close to  $4500 \text{ cm}^{-3}$ .  
148 However, in contrast to the lidar observations, three distinct features are observed: first, the maxima  
149 and minima around the layer peak are much less obvious; second, the peak height of the simulated Na  
150 layer is near 87 km, about 3-4 km lower than the lidar observations, partly due to a few km lower  
151 mesopause in SD-WACCM (Feng et al., 2013); third, the absolute value of Na density vertical gradient



152 below the layer peak is much larger than observed. For instance, the modeled Na density decreases from  
153 near  $4500 \text{ cm}^{-3}$  at 87 km to  $\sim 2000 \text{ cm}^{-3}$  around 82 km, while a similar density decrease is observed by the  
154 lidar to occur between about 95 km and 82 km. Of course, the second and third differences are probably  
155 related. In contrast, Figure 2 (bottom panel) shows that the WACCM-Na high resolution (lev144) output  
156 does capture the three-minima at the layer peak during a diurnal cycle, as observed (Figure 2, top panel).  
157 Although the Na density near the first minimum ( $\sim 4500 \text{ cm}^{-3}$ ) is higher than observed, the times of the  
158 minima, which are close to 20:00 LT, 05:00 LT and 14:00 LT, are in good accord with the lidar  
159 observations. However, the Na peak density ( $> 5500/\text{cm}^3$ ), along with the overall Na column abundance,  
160 is considerably higher than measured by the lidar, and the differences in peak height and vertical density  
161 gradient still persist.

162 In order to examine the density variation on the underside of the layer in greater detail, Figure 3  
163 compares the time-resolved variation of the partial Vertical Column Density (VCD) below 80 km, where  
164 the magnitude of variations is the largest, from the 7-day lidar observations in September 2012 and the  
165 two WACCM-Na simulations. The variation of solar zenith angle is also plotted. Here, due to the  
166 differences of absolute density among the data sets, each VCD is normalized to its maximum so that all  
167 can fit in one plot. There is excellent agreement between the measured and modeled rates of change in Na  
168 VCD around sunrise and sunset. The VCD reaches a maximum around midday and is then fairly constant  
169 in the afternoon. This is because, contrary to the scenario in troposphere, the solar intensity in the  
170 mesosphere is pretty constant during the day. During the night, the Na VCD gradually decays to a  
171 minimum immediately before sunrise. The WACCM lev144 simulation also captures better the observed  
172 rate of decrease of Na immediately after sunset. Note also that the rate of decrease after sunset is faster  
173 than the increase following sunrise. This is caused by the rapid decrease in the concentrations of O and H  
174 at sunset, compared with their slower photochemical buildup (R5-R8) and the photolysis of Na reservoir  
175 species (R1-R4) after sunrise.



176 An interesting contrast can be made with the behavior of the underside of the mesospheric Fe layer,  
177 where considerable density variations due to photolysis have also been observed by Fe lidars within the  
178 similar altitude range [Yu et al., 2012; Viehl et al., 2016]. Also included in Figure 3 is the modeled  
179 variation of the Fe VCD between 75 and 80 km, using a lev144 simulation with WACCM-Fe, which has  
180 been validated against Fe lidar observations [Viehl et al., 2016]. Note that although the rate of decrease of  
181 the Fe VCD around sunset is almost identical to that of Na (because both species correlate with the  
182 falling O and H concentrations after sunset) the rate of increase at sunrise is significantly faster. The Fe  
183 VCD reaches 70% of its daytime maximum within about 1 hour, whereas the Na VCD takes more than 4  
184 hours to reach the same percentage of its maximum.

#### 185 **4. Na variation during solar eclipse**

186 During the solar eclipse on August 21 2017, the USU Na lidar conducted a special campaign to  
187 observe its potential impact on the MLT. The lidar beam was pointed to the north, 30° off zenith, and  
188 operated between 09:45 LT and 15:00 UT. Although this campaign was limited by poor sky conditions in  
189 the early morning and afternoon, it was able to cover the complete course of the solar eclipse and observe  
190 the MLT at the peak of the eclipse with more than 96% of totality at 11:34 LT. To our knowledge, these  
191 are the first lidar observations of the neutral Na in the MLT during an eclipse.

192 Figure 4 shows the lidar-observed variations of mesospheric Na density throughout the eclipse  
193 with 10-minute temporal resolution. The averaged return signal between 200 and 220 km altitude per lidar  
194 Line-of-Sight (LOS) binning range (150 m) is treated as the sky background, which is also shown in  
195 Figure 4. The background variation indicates that at the USU location the eclipse began at 10:25 LT,  
196 peaked at 11:34 LT, and ended just before 13:00 LT. The high background before 10:00 LT was due to  
197 hazy sky condition in the early morning, similar to after 15:00 when it became cloudy. During the course  
198 of this event, the mesospheric Na layer weakened with decreasing peak density. In particular, Na density  
199 variation was more evident below 85 km. As Figure 4 shows, before the eclipse the constant density lines  
200 on the underside of the layer were moving downwards (i.e. increasing density at each altitude). As the



201 eclipse unfolded, these constant density lines started to move towards higher altitudes (the density  
202 decreased at each altitude). During the recovering phase of the eclipse, the Na density began to increase  
203 again. By ~ 13:00 LT, the Na layer was fully recovered, and no significant change was observed on the  
204 underside of the layer. For example, the density line of  $450 \text{ cm}^{-3}$  was near 80 km right before the eclipse  
205 started. It moved upward to near 81.5 km at the culmination of the event, before went back and stayed  
206 near 80 km at the end of the event. Similar behavior can be seen in almost all constant density line below  
207 85 km. Further calculation of the lidar measured underside Na VCD (75-85 km) shows that it decreased  
208 as much as about 40% between 10:25 LT and 11:35 LT.

209 The simultaneous temperature and horizontal wind measurements during the eclipse, however, do not  
210 reveal apparent variations that can be associated with the event (not shown). For instance, the measured  
211 temperature change is within the daytime lidar measurement uncertainty (~ 5K with 4 km smoothing).  
212 Such a small temperature change during the solar eclipse is expected when considering the general  
213 energy budget in the MLT. When the short-wave heating that dominates the daytime budget (mainly  
214 exothermic heating from atomic O recombination is turned off (Brasseur and Solomon, 2005)), infrared  
215 cooling due to  $\text{CO}_2$  emission would lead to net cooling in the mesopause region. However, the magnitude  
216 of this cooling is only about 1 K/hour (Roble, 1995). Thus, for a solar eclipse that only lasts for two hours  
217 with just a few minutes of totality, a noticeable temperature change should not occur. This result is  
218 consistent with a recent simulation of the eclipse using the WACCM-X model, which concluded that the  
219 temperature variation in the mesosphere would have been no more than 4 K [McInerney et al., 2018].  
220 Furthermore, the variation of temperature within this range will not have a significant impact on the Na  
221 reaction kinetics and hence the Na atom density [Plane et al., 1999].

## 222 5. Discussion

223 The major reservoir for Na on the underside of the layer is  $\text{NaHCO}_3$ , which forms by three steps from  
224 Na atoms: oxidation of Na by  $\text{O}_3$  to NaO; reaction with  $\text{H}_2\text{O}$  or  $\text{H}_2$  to form NaOH; and recombination of  
225 NaOH with  $\text{CO}_2$  [Plane et al., 2015; Gomez-Martin et al., 2017].  $\text{NaHCO}_3$  is converted back to Na either



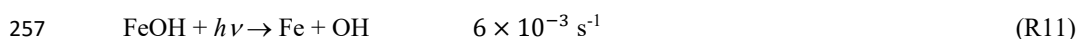
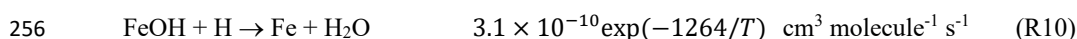
226 by photolysis (reaction R4), or by reaction with atom H in R9. The rate coefficient for this reaction, R9, is  
227  $k_9 = 1.84 \times 10^{-13} T^{0.78} \exp(-1014/T) \text{ cm}^3 \text{ molecule}^{-1} \text{ s}^{-1}$  [Cox et al., 2001], which is  $7.1 \times 10^{-14} \text{ cm}^3$   
228  $\text{ molecule}^{-1} \text{ s}^{-1}$ . The typical daytime H concentration between 75 and 80 km is around  $5 \times 10^7 \text{ cm}^{-3}$  [Plane  
229 et al., 2015], so the first-order rate of this reaction is  $\sim 4 \times 10^{-6} \text{ s}^{-1}$ , which is about 40 times slower than  
230 R4. Thus, photolysis of  $\text{NaHCO}_3$ , which has built up during the night, is responsible for  $\sim 98\%$  of the  
231 increase in the Na VCD after sunrise (Figure 3). The excellent agreement between the laboratory-  
232 measured photolysis rate of  $\text{NaHCO}_3$  [Self and Plane, 2002], and the observed increase of the Na VCD is  
233 strong evidence that  $\text{NaHCO}_3$  is indeed the major Na reservoir on the underside of the Na layer. Indeed,  
234 as shown in Figure 5, the WACCM\_Na simulated variations of Na, H and O, between local midnight and  
235 noon, are highly correlated in the upper mesosphere in the same 144-level run. Within the same region,  
236 the  $\text{NaHCO}_3$  density decreases above 78 km after sunrise due to photolysis and the increases in H and O.  
237 Below this altitude, the change in  $\text{NaHCO}_3$  is much smaller because the concentrations of O and H,  
238 despite increasing after sunrise, are too small to prevent any Na produced being rapidly converted back to  
239  $\text{NaHCO}_3$ . This is because the initial oxidation step – the recombination reaction of Na with  $\text{O}_2$  (which is a  
240 pressure-dependent reaction) – becomes very fast below 78 km.

241 Based on the above discussion, a decrease of Na on the underside of the layer would be expected  
242 during the eclipse, because of the reduction in the photolysis rates (R1-R4) and atomic O and H. As  
243 shown in Figure 4, a decrease in the Na density below 85 km was indeed observed by the lidar during this  
244 period. However, the decrease in Na is relatively small when compared with the natural variability  
245 measured with the USU Na lidar during the morning hours (50 days of lidar data between August 20 and  
246 September 30 in 2011-2016), which can be as much as 60% between 75 and 85 km and is mostly driven  
247 by atmospheric gravity wave modulations [Shelton et al., 1980]. The effect of the eclipse was modeled by  
248 driving a 1D model of the Na layer (0.5 km vertical resolution, 5 min time resolution) [Plane, 2004] with  
249 the background atmospheric species ( $\text{O}_3$ , O, H etc.) from the WACCM-X simulation of the eclipse  
250 [McInerney et al., 2018]. As shown in Figure 6, the modeled decrease in Na around 80 km is much less



251 than the diurnal change in the layer because the period where photolysis is significantly reduced during  
252 the eclipse is too short, and hence within the natural variability of the layer underside.

253 In terms of the mesospheric Fe layer, the major Fe reservoir in this region is most likely FeOH [Self  
254 and Plane 2003; Plane 2004; Plane et al., 2015]. Similar to Na, the dominant Fe production processes  
255 within the bottom half of the layer involve reaction with H and photolysis:



258 The rate coefficients of both these reactions are considerably higher than those of the analogous Na  
259 reactions, particularly R11 which is faster than R4 by more than two orders of magnitude [Viehl et al.,  
260 2016]. It is this feature which controls the more rapid appearance of Fe around 80 km after sunrise, as  
261 shown in Figure 4. Note that this rapid increase has been previously observed by lidar [Viehl et al., 2016;  
262 Yu et al., 2012].

## 263 6. Conclusions

264 Observations of the full diurnal cycle of the underside of the mesospheric Na layer reveal substantial  
265 changes in Na density near and below 80 km, with more than an order-of-magnitude increase after  
266 sunrise, while the change of Na density above 90 km during the same process is relatively slow. In this  
267 study we show that this diurnal variation is largely driven by the photochemistry of the major reservoir  
268 species NaHCO<sub>3</sub>. This result is established by demonstrating reasonable agreement between USU lidar  
269 observations of the Na layer below 80 km, and a whole atmosphere chemistry-climate model which  
270 includes a comprehensive Na chemistry module (WACCM-Na). Indirect photochemistry, where atomic  
271 H and O are produced by the photolysis of O<sub>3</sub>, O<sub>2</sub> and H<sub>2</sub>O, and these atoms then reduce Na compounds  
272 (NaHCO<sub>3</sub>, NaOH, NaO and NaO<sub>2</sub>) back to Na, also plays an important role in the diurnal variability. The  
273 more rapid increase of atomic Fe after sunrise, which has been observed in several locations [Viehl et al.,  
274 2016; Yu et al., 2012], is consistent with the much faster rate of photolysis of FeOH compared with  
275 NaHCO<sub>3</sub>. Lidar observations made during the solar eclipse on August 21, 2017 (at a location with 96%



276 totality) did not reveal significant changes in either temperature or Na density that were larger than the  
277 natural variability around 80 km. This is consistent with a recent study using WACCM-X [McInerney et  
278 al., 2018] and the Na model results presented here.

#### 279 **Acknowledgement:**

280 The lidar work in this study was performed as part of a collaborative research program supported  
281 under the Consortium of Resonance and Rayleigh Lidars (CRRL) National Science Foundation (NSF)  
282 grant AGS1135882, with additional support from NSF grants AGS1734333, and N000141712149 of  
283 Naval Research Laboratory. The lidar data of this study are available at the CRRL Madrigal data base  
284 at: <http://madrigal.physics.colostate.edu/htdocs/>. The National Center for Atmospheric Research is  
285 sponsored by the NSF. JMCP and WF acknowledge funding from the European Research Council  
286 (project number 291332 - CODITA).

#### 287 **Reference:**

- 288 Brasseur, G. P. and Solomon, S., *Aeronomy of the Middle Atmosphere: Chemistry and Physics of the*  
289 *Stratosphere and Mesosphere*, Springer, New York, 2005.
- 290 Carrillo-Sánchez, J. D., D. Nesvorný, P. Pokorný, D. Janches, and J. M. C. Plane, Sources of cosmic dust  
291 in the Earth's atmosphere, *Geophys. Res. Lett.*, 43, 11,979–11,986, doi: 10.1002/2016GL071697, 2016.
- 292 Chen, H., M. A. White, D. A. Krueger, and C. Y. She, Daytime mesopause temperature measurements  
293 using a sodium-vapor dispersive Faraday filter in lidar receiver, *Opt. Lett.*, 21, 1003–1005, 1996.
- 294 Clemesha, D. M., P. P. Batista, D. M. Simonich, Tide-induced oscillations in the atmospheric sodium  
295 layer, *J. Atmos. Terr. Phys.*, 64, 1321–1325, 2002.
- 296 Cox, R.M., D.E. Self and J.M.C. Plane, A study of the reaction between NaHCO<sub>3</sub> and H: apparent  
297 closure on the neutral chemistry of sodium in the upper mesosphere, *Journal of Geophysical Research*,  
298 106, 1733-1739, 2001



- 299 Dawkins, E. C. M., J. M. C. Plane, M. P. Chipperfield, W. Feng, D. R. Marsh, J. Höffner, and D. Janches,  
300 Solar cycle response and longterm trends in the mesospheric metal layers, *J. Geophys. Res. Space*  
301 *Physics*, 121, 7153–7165, doi: 10.1002/2016JA022522, 2016.
- 302 Dunker, T., U.-P. Hoppe, W. Feng, J.M.C. Plane, D.R. Marsh, Mesospheric temperatures and sodium  
303 properties measured with the ALOMAR Na lidar compared with WACCM, *J. Atmos. Sol.-Terr. Phys.*,  
304 127, pp. 111-119, 2015.
- 305 Fan, Z. Y., J. M. C. Plane, J. Gumbel, J. Stegman, and E. J. Llewellyn, Satellite measurements of the  
306 global mesospheric sodium layer, *Atmospheric Chemistry and Physics*, 7, 4107-4115, 2007.
- 307 Feng, W., D. R. Marsh, M. P. Chipperfield, D. Janches, J. Hoeffner, F. Yi, and J. M. C. Plane, A global  
308 atmospheric model of meteoric iron, *J. Geophys. Res. Atmos.*, 118, 9456–9474, 2013.
- 309 Feng, W., Bernd Kaifler, Daniel R. Marsh, Josef Höffner, Ulf-Peter Hoppe, Bifford P. Williams and John  
310 M.C. Plane, Impacts of a sudden stratospheric warming on the mesospheric metal layers, *Journal of*  
311 *Atmospheric and Solar-Terrestrial Physics*, 10.1016/j.jastp.2017.02.004, 162, (162-171), 2017.
- 312 Gómez Martín, J. C., Garraway, S., Plane, J. M. C., Reaction Kinetics of Meteoric Sodium Reservoirs in  
313 the Upper Atmosphere, *Journal of Physical Chemistry A*, 120, 1330-1346, DOI:  
314 10.1021/acs.jpca.5b00622, 2016.
- 315 Gómez Martín, J. C., C. Seaton, M. P. de Miranda, and J. M. C. Plane, The Reaction between Sodium  
316 Hydroxide and Atomic Hydrogen in Atmospheric and Flame Chemistry, *The Journal of Physical*  
317 *Chemistry A* 2017 121 (40), 7667-7674, DOI: 10.1021/acs.jpca.7b07808, 2017.
- 318 Harrell, S. D., C. Y. She, T. Yuan, D. A. Krueger, H. Chen, S. Chen, and Z. L. Hu (2009), Sodium and  
319 potassium vapor Faraday filters re-visited: Theory and applications, *J. Opt. Soc. Am. B*, Vol.26, No.4,  
320 659-670, 2009.
- 321 Hurrell, J. W., J. J. Hack, A. S. Phillips, J. Caron, and J. Yin, The dynamical simulation of the  
322 Community Atmosphere Model version 3 (CAM3), *J. Clim.*, 19, 2162–2183, 2006.



- 323 Kinnison, D. E., et al., Sensitivity of chemical tracers to meteorological parameters in the MOZART-3  
324 chemical transport model, *J. Geophys. Res.*, 112, D20302, doi:10.1029/2006JD007879, 2007.
- 325 Krueger, D. A., C.-Y. She and T. Yuan, Retrieving mesopause temperature and line-of-sight wind from  
326 full-diurnal-cycle Na lidar observations, *Applied Optics* Vol. 54, Iss. 32, pp. 9469-9489, 2015.
- 327 Lamarque, J.-F., Emmons, L. K., Hess, P. G., Kinnison, D. E., Tilmes, S., Vitt, F., Heald, C. L., Holland,  
328 E. A., Lauritzen, P. H., Neu, J., Orlando, J. J., Rasch, P. J., and Tyndall, G. K.: CAM-chem: description  
329 and evaluation of interactive atmospheric chemistry in the Community Earth System Model, *Geosci.*  
330 *Model Dev.*, 5, 369–411, doi:10.5194/gmd-5-369-2012, 2012.
- 331 Langowski, M. P., von Savigny, C., J. P. Burrows, D. Fussen, E. C.M. Dawkins, W. Feng, J. M. C. Plane,  
332 and D. R. Marsh, Comparison of global datasets of sodium densities in the mesosphere and lower  
333 thermosphere from GOMOS, SCIAMACHY and OSIRIS measurements and WACCM model  
334 simulations from 2008 to 2012, *Atmos. Meas. Tech.*, 10, 2989–3006, 2017 [https://doi.org/10.5194/amt-](https://doi.org/10.5194/amt-10-2989-2017)  
335 [10-2989-2017](https://doi.org/10.5194/amt-10-2989-2017), 2017.
- 336 Li, T., Ban, C., Fang, X., Li, J., Wu, Z., Feng, W., Plane, J. M. C., Xiong, J., Marsh, D. R., Mills, M. J., Dou,  
337 X., Climatology of mesopause region nocturnal temperature, zonal wind and sodium density observed by  
338 sodium lidar over Hefei, China (32°N, 117°E), *Atmos. Chem. Phys.*, 18, 11683–11695, doi.org/10.5194/acp-  
339 18-11683-2018, 2018.
- 340 Lin, S.-J., A “vertically-Lagrangian” finite-volume dynamical core for global atmospheric models, *Mon.*  
341 *Weather Rev.*, 132, 2293–2307, 2004.
- 342 Marsh, D. R., Janches, D., Feng, W., & Plane, J. M. C., A global model of meteoric sodium. *Journal of*  
343 *Geophysical Research: Atmospheres*, 118, 11,442–11,452. <https://doi.org/10.1002/jgrd.50870>, 2013.
- 344 McInerney, J. M., Marsh, D. R., Liu, H.-L., Solomon, S. C., Conley, A. J., & Drob, D. P., Simulation of  
345 the 21 August 2017 solar eclipse using the Whole Atmosphere Community Climate Model-eXtended.  
346 *Geophysical Research Letters*, 45, 3793–3800. <https://doi.org/10.1029/2018GL077723>, 2018.



- 347 Merkel, A. W., Marsh, D. R., Gettelman, A., and Jensen, E. J., On the relationship of polar mesospheric  
348 cloud ice water content, particle radius and mesospheric temperature and its use in multi-dimensional  
349 models, *Atmos. Chem. Phys.*, 9, 8889-8901, <https://doi.org/10.5194/acp-9-8889-2009>, 2009.
- 350 Neale, R., J. Richter, S. Park, P. Lauritzen, S. Vavrus, P. Rasch, and M. Zhang, The mean climate of the  
351 Community Atmosphere Model (CAM4) in forced SST and fully coupled experiments, *J. Clim.*, 26(14),  
352 5150–5168, doi:10.1175/JCLI-D-12-00236.1, 2013.
- 353 Plane, J. M., C. S. Gardner, J. Yu, C. Y. She, R. R. Garcia and H. C. Pumphrey, Mesospheric Na layer at  
354 40N: Modeling and observations, *J. Geophys. Res.*, 104, NO. D3, 3773-3788, 1999.
- 355 Plane, J. M. C., Atmospheric chemistry of meteoric metals, *Chem. Rev.*, 103(12), 4963–4984,  
356 doi:10.1021/cr0205309, 2003.
- 357 Plane, J. M. C., A time-resolved model of the mesospheric Na layer: Constraints on the meteor input  
358 function. *Atmospheric Chemistry and Physics*, 4, 627–638. <https://doi.org/10.5194/acp-4-627-2004>,  
359 2004.
- 360 Plane, J. M. C., et al. (2014), A combined rocket-borne and ground-based study of the sodium layer and  
361 charged dust in the upper mesosphere, *J. Atmos. Sol. Terr. Phys.*, 118, 151–160, 2014.
- 362 Plane, J. M. C., W. Feng, and E. C. M. Dawkins, The mesosphere and metals: Chemistry and changes,  
363 *Chem. Rev.*, doi:10.1021/cr5, 2015.
- 364 Roble, R. G., Energetics of the mesosphere and thermosphere, R. M. Johnson, T. L. Killeen (Eds.), *The*  
365 *Upper Atmosphere and Lower Thermosphere: A Review of Experiment and Theory*, American  
366 Geophysical Union, Washington, DC, 1995.
- 367 Sandford, M. C. W., and A. J. Gibson, Laser radar measurements of the atmospheric sodium layer, *J.*  
368 *Atmos. Terr. Phys.*, 32, 1423-1430, 1970.



- 369 Shelton, J. D., C. S. Gardner, and C. F. Sechrist, Jr., Density response of the mesospheric sodium layer to  
370 gravity wave perturbations, *Geophys. Res. Lett.*, 7, 1069-1072, 1980.
- 371 Self, D. E. and J. M. C. Plane, Absolute photolysis cross-sections for  $\text{NaHCO}_3$ ,  $\text{NaOH}$ ,  $\text{NaO}$ ,  $\text{NaO}_2$  and  $\text{NaO}_3$  :  
372 implications for sodium chemistry in the upper mesosphere, *Phys. Chem. Chem. Phys.*, 4, 16-23, doi:  
373 10.1039/B107078A, 2002.
- 374 Self, D. E., and J. M. C. Plane, A kinetic study of the reactions of iron oxides and hydroxides relevant to  
375 the chemistry of iron in the upper mesosphere, *Phys. Chem. Chem. Phys.*, 5, 1407–1418, doi:10.1039/  
376 b211900e, 2003.
- 377 States, R. J., Gardner, C. S., Structure of mesospheric Na layer at 40N latitude: seasonal and diurnal  
378 variations. *J. Geophys. Res.*, 104, 11783-11798, 1999.
- 379 Viehl, T. P., J. M. C. Plane, W. Feng, and J. Höffner, The photolysis of  $\text{FeOH}$  and its effect on the  
380 bottomside of the mesospheric Fe layer, *Geophys. Res. Lett.*, 43, 1373–1381, doi:  
381 10.1002/2015GL067241, 2016.
- 382 Yu, Z., X. Chu, W. Huang, W. Fong, and B. R. Roberts, Diurnal variations of the Fe layer in the  
383 mesosphere and lower thermosphere: Four season variability and solar effects on the layer bottomside at  
384 McMurdo (77.8°S, 166.7°E), Antarctica, *J. Geophys. Res.*, 117, D22303, doi:10.1029/2012JD018079,  
385 2012.
- 386 Yuan, T., She, C.-Y., Kawahara, T. D., & Krueger, D. A., Seasonal variations of mid-latitude  
387 mesospheric Na layer and its tidal period perturbations based on full-diurnal-cycle Na lidar observations  
388 of 2002–2008. *J. Geophys. Res.*, 117, D1130, <https://doi.org/10.1029/2011JD017031>, 2012.
- 389 Yuan, T., She, C. Y., Oberheide, J., & Krueger, D. A., Vertical tidal wind climatology from full-diurnal-  
390 cycle temperature and Na density lidar observations at Ft. Collins, CO (41°N, 105°W). *J. Geophys. Res.*:  
391 *Atmo.*, 119, 4600–4615, <https://doi.org/10.1002/2013JD020338>, 2014b.



393 **Figure Captions:**

394 Figure 1. The Na density ( $\text{cm}^{-3}$ ) variation between 75 km and 105 km in MLT during sunrise between  
395 August 20<sup>th</sup> and September 30<sup>th</sup> (contour plot) in 2011-2016. Zero hour marks time of the sunrise at the  
396 mesopause (bottom abscissa). The solid black profile is the ratio between the Na density 3 hours after  
397 sunrise to that 3 hours before sunrise (top abscissa).

398 Figure 2. The averaged lidar measured Na density variation during the 7-day Na lidar campaign between  
399 September 27 and October 3, 2012 (top); the Na density variations at USU location during the same time  
400 frame simulated by WACCM\_Na 88-level (middle) and 144-level (bottom).

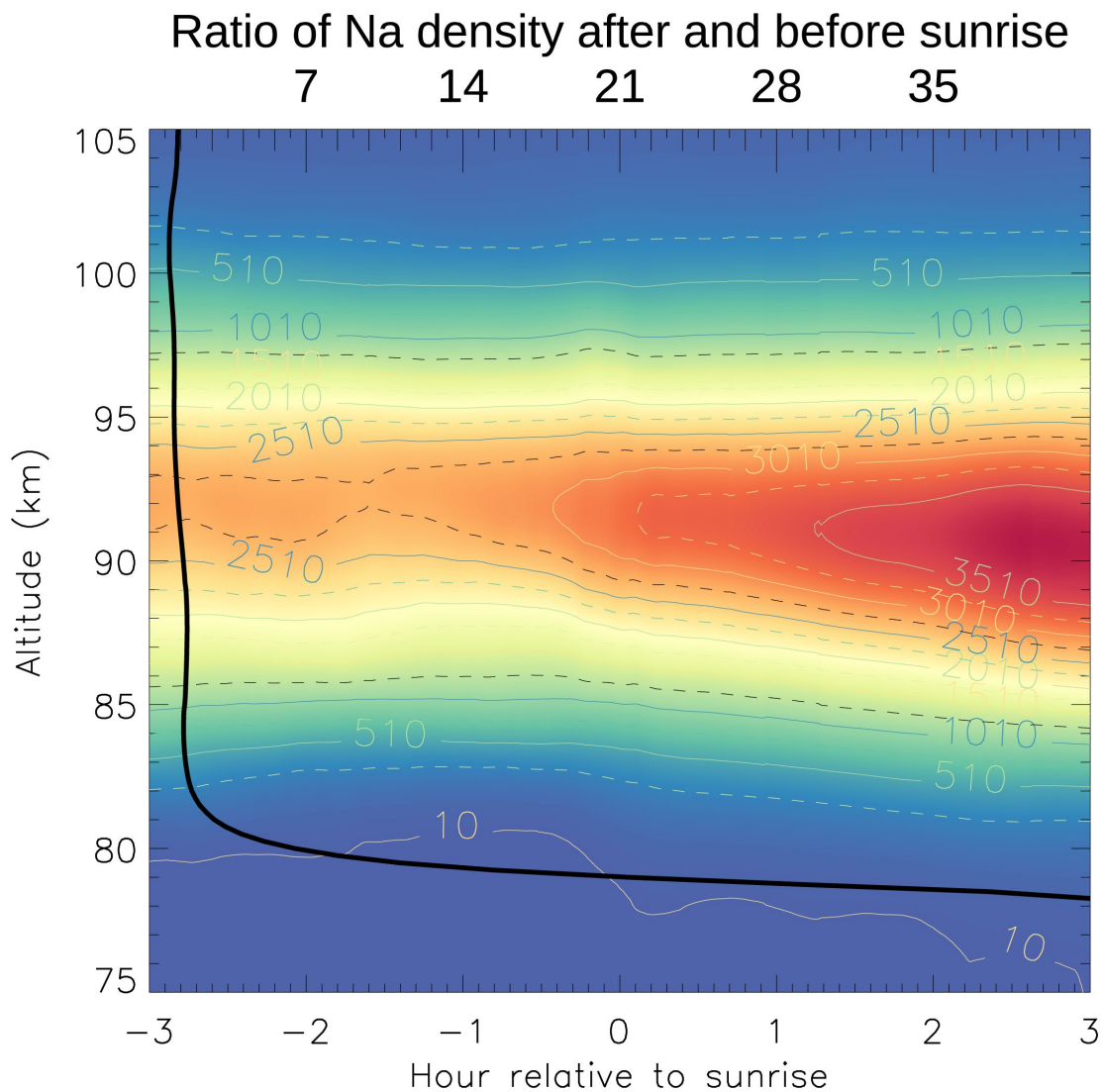
401 Figure 3. The variations of Na VCD (75-80 km) measured the USU Na lidar during the 7-day Na lidar  
402 campaign (asterisks), simulated by WACCM\_Na 88-level run (orange dotted line) and 144-level run  
403 (orange dashed line) and solar zenith angle (black long-dashed line), along with Fe VCD (75-80 km)  
404 simulated by WACCM\_Fe 144-level run (blue solid line).

405 Figure 4. The mesospheric Na density variation during the solar eclipse on August 2, 2017, observed by  
406 the Na lidar at Utah State University. The yellow solid line represents the lidar-detected sky background.  
407 The unit for the lidar background measurement is #photon/bin/minute.

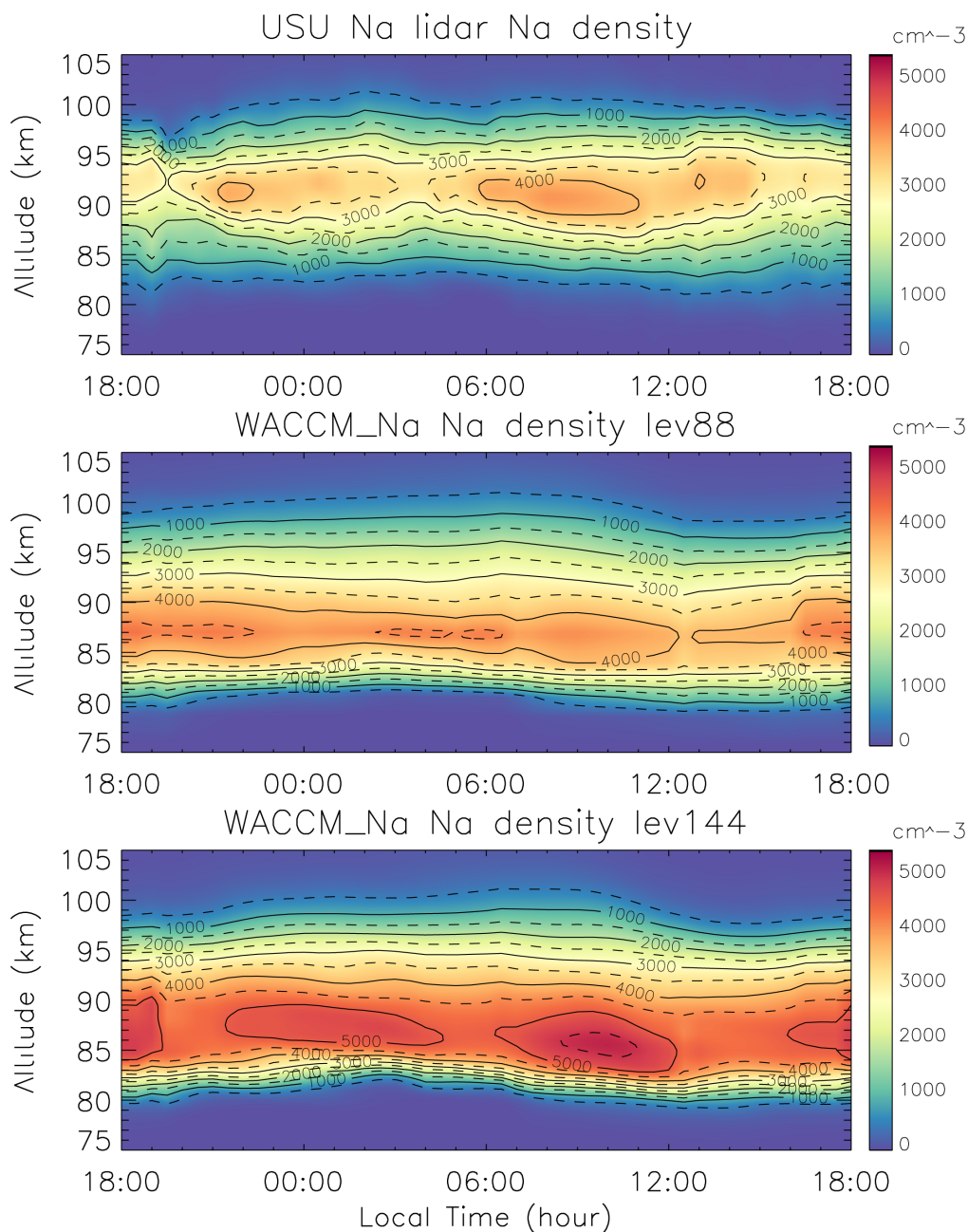
408 Figure 5. The variations of Na (a), NaHCO<sub>3</sub>(b), H(c) and O(d) in the underside of the mesospheric Na  
409 layer, simulated by WACCM\_Na\_144-level run.

410 Figure 6. A 1D model simulation of the Na layer variation during the solar eclipse between 18:00 LT on  
411 August 20 and 18:00 LT on August 21 in 2017. The solar eclipse at the USU Na lidar location peaked at  
412 11:34 on August 21 (marked by the solid arrow). The background atmospheric species (O<sub>3</sub>, O, H etc.) are  
413 based on the outputs of WACCM-X eclipse simulation.

414



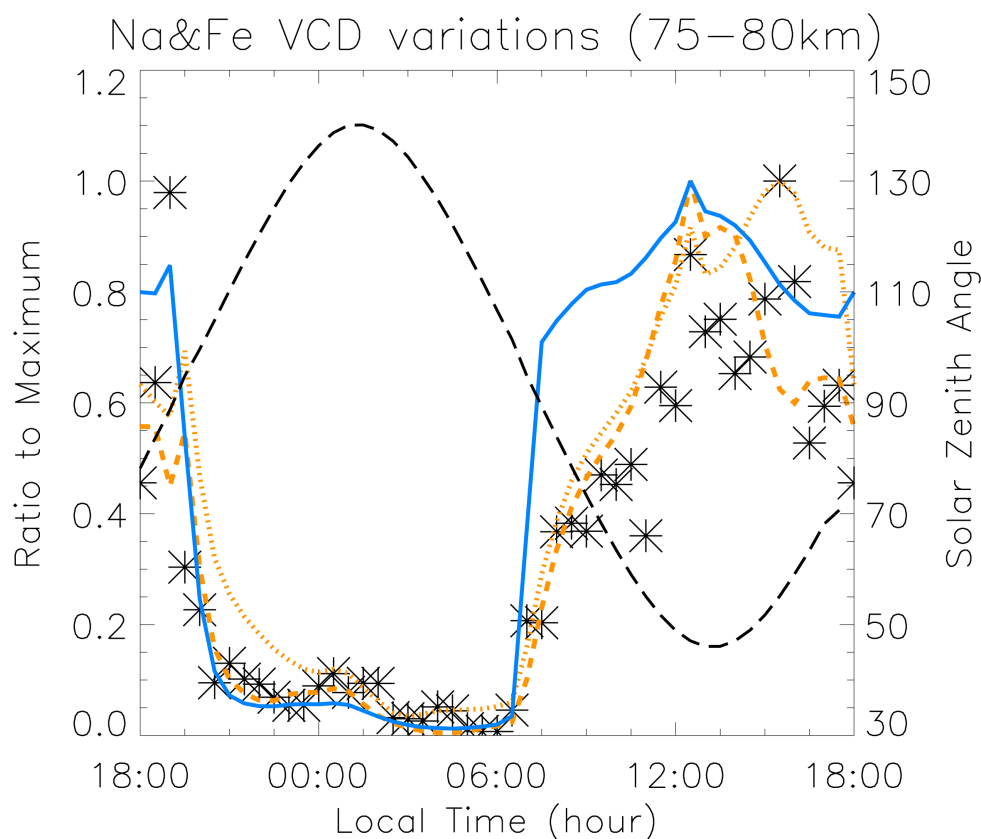
415  
416 Figure 1. The Na density ( $\text{cm}^{-3}$ ) variation between 75 km and 105 km in MLT during sunrise between  
417 August 20<sup>th</sup> and September 30<sup>th</sup> (contour plot) in 2011-2016. Zero hour marks time of the sunrise at the  
418 mesopause (bottom abscissa). The solid black profile is the ratio between the Na density 3 hours after  
419 sunrise to that 3 hours before sunrise (top abscissa).



420

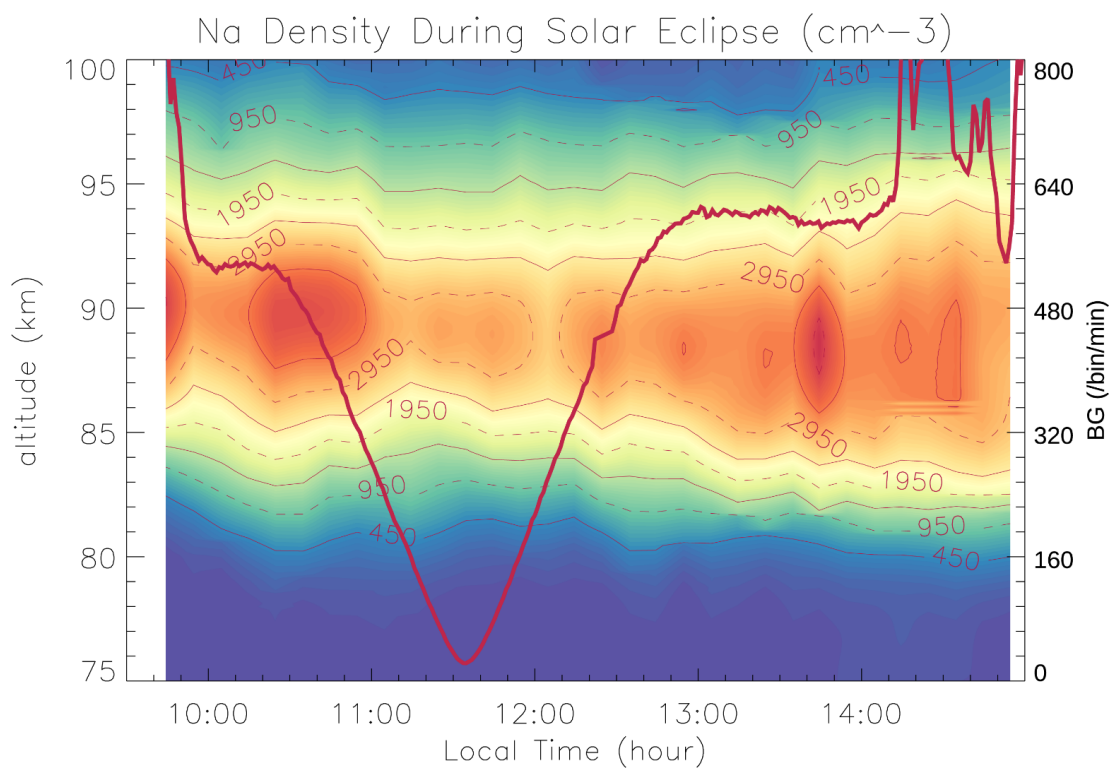
421 Figure 2. The averaged lidar measured Na density variation during the 7-day Na lidar campaign between  
422 September 27 and October 3 2012 (top); the Na density variations at USU location during the same time  
423 frame simulated by WACCM\_Na 88-level (middle) and 144-level (bottom).

424



425

426 Figure 3. The variations of Na VCD (75-80 km) measured the USU Na lidar during the 7-day Na lidar  
427 campaign (asterisks), simulated by WACCM\_Na 88-level run (orange dotted line) and 144-level run  
428 (orange dashed line) and solar zenith angle (black long-dashed line), along with Fe VCD (75-80 km)  
429 simulated by WACCM\_Fe 144-level run (blue solid line).

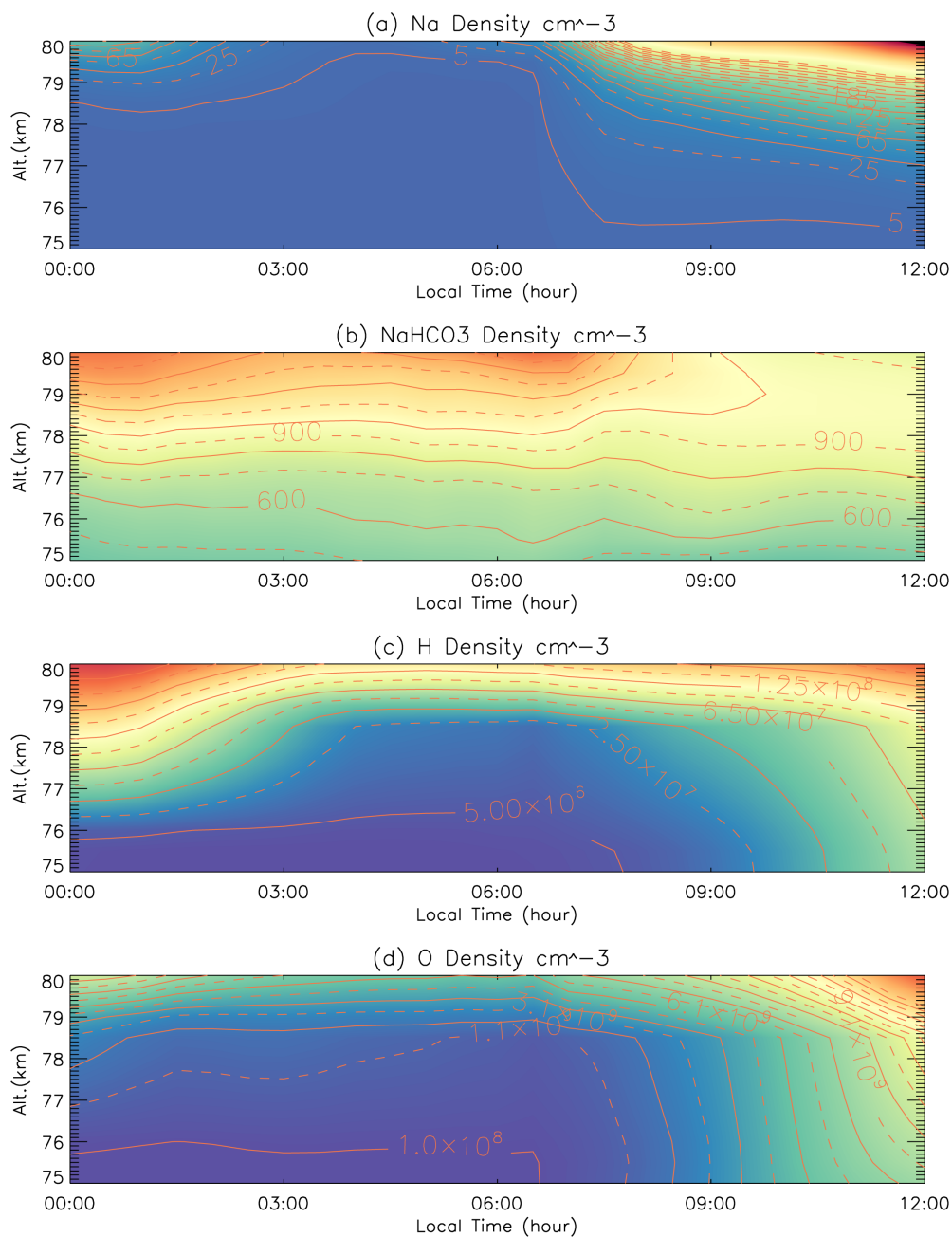


430

431 Figure 4. The mesospheric Na density variation during the solar eclipse on August 2, 2017, observed by  
 432 the Na lidar at Utah State University. The yellow solid line represents the lidar-detected sky background.

433 The unit for the lidar background measurement is #photon/bin/minute.

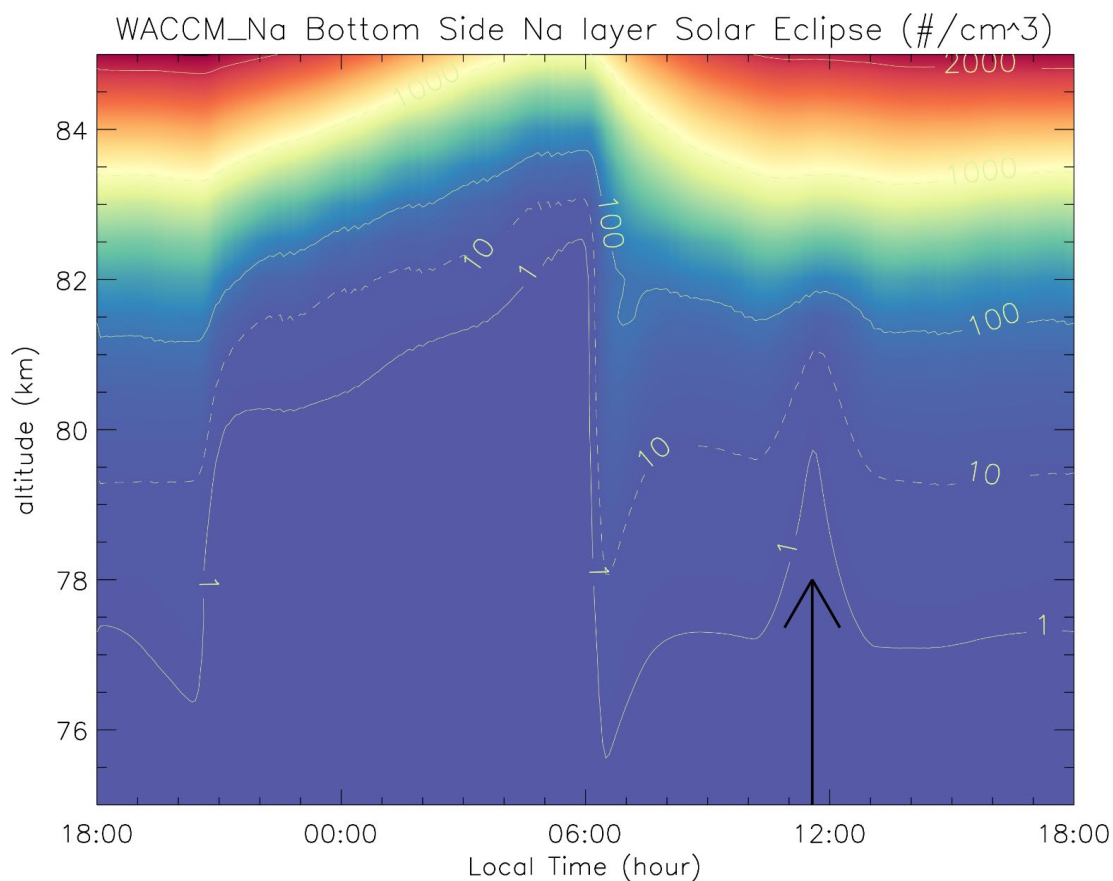
434



435

436 Figure 5. The variations of Na (a),  $\text{NaHCO}_3$ (b), H(c) and O(d) in the underside of the mesospheric Na

437 layer, simulated by WACCM\_Na\_144-level run.



438

439 Figure 6. A 1D model simulation of the Na layer variation during the solar eclipse between 18:00 LT on  
440 August 20 and 18:00 LT on August 21 in 2017. The solar eclipse at the USU Na lidar location peaked at  
441 11:34 on August 21 (marked by the solid arrow). The background atmospheric species ( $O_3$ , O, H etc.) are  
442 based on the outputs of WACCM-X eclipse simulation.

443